

Strongly anisotropic spin relaxation in graphene/WS₂ van der Waals heterostructures

L. A. Benitez^{1,2,*} J. F. Sierra^{1,†} W. Savero Torres^{1,†} A.

Arrighi^{1,2}, F. Bonell¹, M. V. Costache¹, and S. O. Valenzuela^{1,3‡}

¹*Catalan Institute of Nanoscience and Nanotechnology (ICN2),
CSIC and The Barcelona Institute of Science and Technology (BIST),
Campus UAB, Bellaterra, 08193 Barcelona, Spain*

²*Universitat Autònoma de Barcelona,
Bellaterra, 08193 Barcelona, Spain and*

³*Institució Catalana de Recerca i Estudis Avançats (ICREA), 08070 Barcelona, Spain*

Abstract

Graphene has emerged as the foremost material for future two-dimensional spintronics due to its tuneable electronic properties [1–3]. In graphene, spin information can be transported over long distances [4] and, in principle, be manipulated by using magnetic correlations or large spin-orbit coupling (SOC) induced by proximity effects [3, 5]. In particular, a dramatic SOC enhancement has been predicted when interfacing graphene with a semiconducting transition metal dichalcogenide [6], such as tungsten disulphide (WS₂). Signatures of such an enhancement have recently been reported [7–10] but the nature of the spin relaxation in these systems remains unknown. Here, we unambiguously demonstrate anisotropic spin dynamics in bilayer heterostructures comprising graphene and WS₂. By using out-of-plane spin precession [11, 12], we show that the spin lifetime is largest when the spins point out of the graphene plane. Moreover, we observe that the spin lifetime varies over one order of magnitude depending on the spin orientation, indicating that the strong spin-valley coupling in WS₂ is imprinted in the bilayer and felt by the propagating spins. These findings provide a rich platform to explore coupled spin-valley phenomena and offer novel spin manipulation strategies based on spin relaxation anisotropy in two-dimensional materials.

* antonio.benitez@icn2.cat

† These authors contributed equally to this work

‡ SOV@icrea.cat

Monolayers of semiconducting transition metal dichalcogenides (TMDC) have a sizable band gap of about 1 - 2 eV. Their crystal structure lacks an inversion centre, resulting in valence and conduction bands in nonequivalent valleys at the K and K' points of the Brillouin zone [13]. Because of the heavy atoms and outer d -orbitals, the SOC and associated spin splitting are large and the spin and valley degrees of freedom are strongly coupled [14–17]. The spin-valley coupling suppresses both spin and valley relaxation, providing a new means of controlling the valley polarization through spin injection or vice versa [16].

First principle calculations have shown that TMDCs can induce a large SOC in graphene in the meV range while preserving the graphene linear Dirac band structure [6, 18]. Enhancement of the SOC has been demonstrated using non-local charge transport and weak (anti-)localization measurements [7–10, 19], the most salient signature of the SOC being a drastic reduction of the spin lifetime down to the picosecond range [8–10, 19]. In recent spin transport experiments, the spin sink effect in the TMDCs was used to modulate the transmission of pure spin currents [9, 10]. This enabled the realization of a spin field-effect switch that changed between “on” and “off” by gate tuning.

A further consequence of the proximity-induced SOC, which has not been addressed experimentally, is a strong spin-valley coupling imprinted by the TMDC to graphene. As depicted in Fig. 1a, a band gap is expected to open in the Dirac cone of graphene due to the breaking of pseudospin symmetry, while the SOC, combined with broken space inversion symmetry, removes the spin degeneracy of the conduction and valence bands [6, 18]. The spins in these bands tilt out of the graphene plane, with the out-of-plane component alternating from up to down as the energy of the bands increases, in a sequence that inverts between K and K' . The spin splitting implies that the spin dynamics would likely differ for spins pointing in (\parallel) and out of (\perp) the graphene plane, leading to distinct spin lifetimes, τ_s^{\parallel} and τ_s^{\perp} . Indeed, realistic modelling and numerical simulations in graphene(gr)/WS₂ predict that the spin lifetime anisotropy ratio $\zeta \equiv \tau_s^{\perp}/\tau_s^{\parallel}$ could reach values as large as a few hundreds, in the presence of intervalley scattering [20]. In other words, the recently proposed gr/TMDC spin switch [9, 10] should actually behave as a filter for spin currents, with a transmission that depends on the orientation of the spins relative to the plane. Quantification of ζ can therefore provide unique insight to spin-valley coupling mechanisms and help elucidate the nature of the induced SOC [1, 11].

Recent experiments have demonstrated that ζ can readily be determined combining in-

plane and out-of plane spin precession measurements [11, 12]. In order to reveal the spin-valley coupling in gr/WS₂, we implement such a technique using the device depicted in Fig. 1b. The measurements are based on the standard non-local spin injection and detection technique [21, 22]. A WS₂ flake is placed over the graphene spin channel between the ferromagnetic injector (F1) and detector (F2) electrodes, creating a gr/WS₂ van der Waals heterostructure (see Methods and Supplementary Fig. 1). The WS₂ locally modifies the graphene band structure by proximity effect and, as a consequence, the spin diffusion. Considering that τ_s^{\parallel} in the modified graphene region is expected to be in the range of a few ps [10, 20], the spin relaxation length should be in the submicron range. The width w of the WS₂ flake is thus selected to be about one micrometre so as to avoid suppressing the spin population completely when spins are in-plane. The spin channel length L , which is defined as the distance between F1 and F2, is much longer than w (about 10 μm) to ensure that the spin precession response of the device can be studied at moderate magnetic fields [11, 12]. A gate voltage applied to the substrate ($p\text{Si}/\text{SiO}_2$) is used to tune the spin sink in WS₂ [9, 10]. For reasons that will become clear later, the WS₂ flake is off-centre and close to F2. All the experiments are performed at room temperature.

Owing to magnetic shape anisotropy, the magnetizations of F1 and F2 tend to remain in-plane. An out of plane magnetic field B , which causes spins to precess exclusively in plane, will sense τ_s^{\parallel} only. In order to obtain information on τ_s^{\perp} , we follow two strategies represented in Figs. 1c and 1d. The strategies, which are described in [11, 12], rely on the application of an oblique B characterized by an angle β (Fig. 1c) or an in-plane B perpendicular to the easy magnetization axes of F1/F2 (Fig. 1d). As represented by the red arrows, such magnetic fields cause the spins to precess out of the graphene plane as they diffuse towards the detector. When a spin reaches the gr/WS₂ region, its orientation is characterized by the angle β^* , which denotes the inclination of the spin from the graphene plane and depends on the magnitude of B (Fig. 1b). The spin precession dynamics therefore becomes sensitive to both τ_s^{\parallel} and τ_s^{\perp} , and then τ_s^{\perp} can be determined. If the spin lifetime in gr/WS₂ is anisotropic, the transmission of the spins across this region will be modulated by B .

Figure 2 demonstrates the changes in the spin precession lineshape, R_{nl} vs B , induced by the presence of the WS₂ in the spin channel. The non-local spin resistance $R_{\text{nl}} = V_{\text{nl}}/I$ is determined from the non-local voltage V_{nl} at the detector F2 that is generated by a

current I flowing at the injector F1 (Fig. 1b). Figures 2a to 2c show measurements for a typical gr/WS₂ device. Figures 2d to 2f show the corresponding measurements for a standard graphene device (without WS₂), which was fabricated in the same graphene flake as a reference (see Supplementary Fig. 1). The data are acquired for parallel and antiparallel magnetization configuration of the electrodes. Notably, the spin precession response in the two devices displays different behaviour. Figures 2a and 2d present conventional spin precession measurements with an out-of-plane magnetic field. Even though spin precession is observed in both cases, the magnitude of the signal in Fig. 2a is two orders of magnitude smaller than in Fig. 2d. Such a decrease indicates a large reduction of the in-plane spin relaxation length λ_s^{\parallel} in the gr/WS₂ region, as observed previously for MoS₂ [10].

Figures 2b and 2e present spin precession measurements for in-plane B , as shown in Fig. 1d. While the change in magnetic field configuration results in no significant variation in the reference device (compare Figs. 2d and 2e), the changes observed in the gr/WS₂ device are remarkable (see Figs. 2a and 2b). Figure 2b shows that, as $|B|$ increases, $|R_{nl}|$ becomes much larger than its value at $B = 0$. The anomalous enhancement of $|R_{nl}|$ is a clear indication of anisotropic spin relaxation, with an out-of-plane spin relaxation length λ_s^{\perp} larger than λ_s^{\parallel} and thus $\zeta > 1$.

The difference between Figs. 2d and 2e is due to the tilting of the electrodes magnetization with B . In both experiments, B is perpendicular to the equilibrium magnetization at $B = 0$, however the tilting is pronounced when B is oriented in plane for which the shape anisotropy is small. In an isotropic system, the non-local resistance has the form [12, 22] $R_{nl}^{\pm} = [\pm g(B) \cos^2 \gamma + \sin^2 \gamma] R_{nl,0}$ for initially parallel (+) and antiparallel (-) configurations of the F1/F2 magnetizations, with $g(B)$ a function that captures the precession response, γ the tilting angle of the F1/F2 magnetizations and $R_{nl,0} = R_{nl}(B = 0)$. By noting that $\Delta R_{nl} = R_{nl}^{+} - R_{nl}^{-} = 2g(B) R_{nl,0} \cos^2 \gamma$, it is evident that for an isotropic system and small γ , ΔR_{nl} is independent of the orientation of B . The obtained ΔR_{nl} for the two B orientations are shown in Figs. 2c and 2f for the gr/WS₂ and the reference device, respectively. The nearly perfect overlap of the two curves in Fig. 2f is a consequence of the isotropic spin relaxation in graphene [11, 12]. The disparity of the curves in Fig. 2c demonstrates the highly anisotropic nature of the spin transport in gr/WS₂. The extrema in R_{nl} in Fig. 2b are reached when the aggregate orientation of the diffusing spins have rotated by $\pi/2$ at the WS₂ location. Because the diffusing spins reach WS₂ slightly before F2, the extrema occur

at magnetic fields that are slightly larger than those at which $R_{\text{nl}} = 0$ in the conventional spin precession measurements (dashed vertical lines in Fig. 2c).

The decrease in the magnitude of R_{nl} observed between Figs. 2c and 2a is systematically found in all of our devices. It is a direct consequence of the small spin relaxation length λ_s^{\parallel} in gr/WS₂, which can be determined by solving the diffusive Bloch equations (Supplementary Information). At $B = 0$ the solution in z , along the graphene flake, for a specific region (r) of the device has the general form $A_r e^{z/\lambda_{s,r}} + B_r e^{-z/\lambda_{s,r}}$ with A_r, B_r determined by the boundary conditions and $\lambda_{s,r}$ the spin relaxation length, which in gr/WS₂ is λ_s^{\parallel} and in graphene $\lambda_{s,\text{gr}}$. The latter is assumed to be equal to that in the reference device, as extracted from conventional spin precession results as in Fig. 2b. From the change in $R_{\text{nl},0}$ between the gr/WS₂ and reference devices, λ_s^{\parallel} is estimated to be about 0.2-0.4 μm , which is significantly smaller than the typical $\lambda_{s,\text{gr}} \sim 3\text{-}5 \mu\text{m}$.

Figure 2 shows that the out-of-plane spin component is transmitted through gr/WS₂ much more efficiently than the in-plane component. Thus, gr/WS₂ acts as a filter with a transmission that depends on the effective orientation of the spins that reach it. Such a filter represents a new tool in spintronics to detect small variations in the orientation of spins arriving to it. In the device of Fig. 2, a difference in transmission of one order of magnitude is estimated by comparing the extrema in $|R_{\text{nl}}|$ in the two B configurations.

Having determined λ_s^{\parallel} , the anisotropy can be estimated by using out-of-plane precession with oblique B . Because the carrier motion towards WS₂ is diffusive, the spins are characterized by a broad distribution of inclination angles β^* (Fig. 1a). As B increases, the spin component perpendicular to the magnetic field dephases and only the component parallel to the field contributes to R_{nl} [11]. In the case depicted in Fig. 1c, this component is non-zero and the spin orientation is univocally determined by $\beta^* = \beta$, which greatly simplifies the analysis to obtain ζ . Indeed, the effective spin relaxation length in gr/WS₂ for any given β , λ_s^{β} , can be calculated using the same procedure that was used to find λ_s^{\parallel} (Supplementary Information).

To achieve full dephasing at moderate B , the WS₂ flake is located close to the ferromagnetic electrode that typically plays the role of detector (F2 in Fig. 1b). Figure 3a shows spin precession measurements for a representative set of β values in a device with distances $L = 11 \mu\text{m}$ between F1 and F2, and $L_1 = 7.5 \mu\text{m}$ between F1 and WS₂ (Fig. 1b). A back gate of -15 V was applied in order to suppress the spin sink effect in WS₂. It is observed that

the diffusive broadening dephases the precessional motion at $B_d \sim 0.12$ T. For $B > B_d$, R_{nl} is nearly constant with increasing B , with a magnitude $R_{nl}^\beta \equiv R_{nl}(B > B_d)$. At $\beta = 90^\circ$, the response is similar to that found in conventional spin precession measurements in graphene (as in Fig. 2a). As soon as the magnetic field is tilted from the perpendicular orientation, R_{nl}^β increases anomalously, and even a few degrees tilt results in R_{nl}^β values that are larger than $R_{nl,0}$ even at small B (see, for example, the response at $\beta = 85.5^\circ$). This is in stark contrast to the case of pristine graphene. Equivalent measurements for the reference device are shown in Supplementary Fig. 4, there $\zeta \approx 1$ and $R_{nl,0}$ is an upper limit for R_{nl} [11].

As a comparison, Fig. 3b shows measurements as those in Fig. 3a with the role of F1 and F2 reversed. Because the injector (F2) is now close to WS_2 , the aggregate spin precession angle at the WS_2 location is smaller than in Fig. 3a for any given B . Full dephasing at gr/ WS_2 is not achieved, even at the largest B , while R_{nl} does not reach the largest values observed in Fig. 3a, which implies that the spins do not fully rotate out of plane.

For a generic anisotropic spin channel, R_{nl}^β can be written as $R_{nl}^\beta = \overline{R_{nl}^\beta} \cos^2(\beta - \gamma)$, where $\overline{R_{nl}^\beta}$ is the nonlocal resistance that would be measured if the magnetization of the injector and detector were along the magnetic field. The factor $\cos^2(\beta - \gamma)$ thus accounts for the projection of the injected spins along B and the subsequent projection along the direction of the detector magnetization [11]. For $\zeta = 1$, $\overline{R_{nl}^\beta} = R_{nl,0}$, regardless of the value of β and, therefore, plotting R_{nl}^β versus $\cos^2(\beta - \gamma)$ results in a straight line. For $\zeta \neq 1$, R_{nl}^β lies above or below the straight line depending whether $\zeta > 1$ or $\zeta < 1$ (Fig. 4a)[11].

The magnitude of $R_{nl}^\beta \equiv R_{nl}(B > B_d)$ normalized to $R_{nl,0}$ is shown in Fig. 4a as a function of $\cos^2(\beta - \gamma)$ both for the gr/ WS_2 and the reference device (full and open symbols, respectively). The angle γ is calculated from the fittings to the spin precession in the reference, using the conventional non-local spin precession method [11]. The data for the gr/ WS_2 and the reference devices were extracted from Fig. 3a and Supplementary Fig. 4, respectively. Consistent with the results in Fig. 2, $\zeta \approx 1$ for the reference device, while $\zeta \gg 1$ for gr/ WS_2 .

In order to verify that the anisotropy is driven by proximity SOC, we have tuned the spin sink effect by changing the gate voltage V_g , which controls the carrier density in both graphene and WS_2 . Figure 4b shows the obtained $\overline{R_{nl}^\beta}$ versus β as a function of V_g . Below a threshold gate voltage $V_g^T \sim -5$ V, $\overline{R_{nl}^\beta}$ is independent of V_g . However, for $V_g > V_g^T$, a rapid reduction of $\overline{R_{nl}^\beta}$ is observed for all values of β . For $V_g > 10$ V, no spin signal can be

detected when the spins are oriented in-plane; the spin signal is recovered as soon as the spin component out of plane is non zero, indicating that $\zeta \gg 1$.

A strong modulation and vanishing of R_{nl} with the application of positive V_g were recently reported in gr/MoS₂ heterostructures [9, 10]. There, spins were oriented in-plane and the change in the spin transport properties was attributed to the gate tuning of the MoS₂ channel conductivity and associated modulation of the Schottky barrier at the MoS₂/graphene interface [9, 10]. The inset of Fig. 4b shows the bias characteristics of our gr/WS₂ device. The current I_{ds} is measured versus V_g when a driving voltage V_{ds} is applied between graphene and WS₂. The response is very similar to that reported in Refs. [9, 10], with I_{ds} increasing dramatically nearby V_g^{T} , which indicates that the suppression in the spin signal for $V_g > V_g^{\text{T}}$ is due to a fast relaxation of spins as they enter WS₂, as observed with MoS₂. The fact that $\overline{R_{\text{nl}}^{\beta}}$ is independent of V_g and that the carriers cannot enter WS₂ below V_g^{T} confirms that the anisotropic spin relaxation is due to proximity-induced SOC.

The spin anisotropy ratio ζ can be obtained from the in-plane and out-of-plane spin relaxation lengths as $\zeta = (\lambda_s^{\perp}/\lambda_s^{\parallel})^2$. From $\overline{R_{\text{nl}}^{\beta}} \sim 1.5 \Omega$ with β approaching 90° , we obtain $\lambda_s^{\perp} \sim 1 \mu\text{m}$. Taking $\lambda_s^{\parallel} \sim 0.3 \mu\text{m}$, we find $\zeta \approx 10$. Assuming that the diffusion constant in gr/WS₂ is of similar magnitude to that in graphene, $D \sim 0.03 \text{ m}^2\text{s}^{-1}$ then $\tau_s^{\parallel} \sim 3 \text{ ps}$ and $\tau_s^{\perp} \sim 30 \text{ ps}$. Using these parameters we can directly estimate R_{nl}^{β} versus $\cos^2(\beta - \gamma)$ (see Supplementary Information). The results of the calculations are displayed in Fig. 4a (solid green line), showing very good agreement with the experimental results, given that no adjustable parameters were used. Furthermore, R_{nl}^{β} for any given value of B can be found by solving the diffusive Bloch equation in the presence of an oblique magnetic field [12]. Supplementary Figs. 2 and 3 show the calculated R_{nl}^{β} for a homogeneous gr/WS₂ structure both for oblique and in-plane B . The general agreement between Figs. 2c and 3a with Supplementary Figs. 2a and 3, respectively, gives further confidence to the interpretation of our results.

The in-plane spin lifetime τ_s^{\parallel} is of similar magnitude than that found in gr/MoS₂ with conventional spin precession measurements, $\tau_s \sim 5 \text{ ps}$ [10]. It is also very close to that extracted by weak anti-localization experiments in gr/WS₂, $\tau_s \sim 2.5\text{-}5 \text{ ps}$ [8, 19]. These experiments however do not provide information on the mechanisms governing the spin dynamics, as extracted from the spin relaxation anisotropy. Spin dynamics modelling and numerical simulations have been used to compute ζ in graphene interfaced with several

TMDCs [20]. In the case of strong intervalley scattering, ζ in gr/WS₂ was calculated to be between 20 to 200, with $\tau_s^{\parallel} \sim 1$ ps and $\tau_s^{\perp} \sim 20$ to 200 ps, while in the absence of intervalley scattering, ζ decreases all the way down to 1/2, as expected with Rashba SOC, with $\tau_s^{\parallel} \approx 2\tau_s^{\perp} \sim 10$ ps near the charge neutrality point. The large ζ is therefore not only a fingerprint of SOC proximity effects induced by WS₂ but also indicates that intervalley scattering in our devices is important. The somewhat smaller ζ found in the experiments can originate from a number of reasons, the most straightforward being that the intervalley scattering is stronger in our devices than the assumed in the calculations. This is supported by the fact that the experimental τ_s^{\parallel} and τ_s^{\perp} fall both in-between the extremes estimated for the strong intervalley and no-intervalley scattering regimes [20]. There are other possibilities. Because the obtained λ_s^{\perp} is similar to the width w of gr/WS₂, our approach could become insensitive for large values of ζ . However, calculations shown in Supplementary Fig. 5 show that this limit has not been reached, in particular when B is tilted slightly from the perpendicular orientation. Another aspect to be considered is the relevance of intravalley scattering and how it compares with intervalley scattering. Our measurements are all carried out at room temperature, phonon scattering can increase the weight of intravalley scattering and effectively reduce the anisotropy.

Our results therefore demonstrate that the large SOC in a semiconducting transition metal dichalcogenide, which leads to spin-valley coupled dynamics, can be directly imprinted in graphene by means of a van der Waals heterostructure. Studying the spin lifetime anisotropy not only provides insight into the physics underpinning spin and valley dynamics in these systems but also opens the door for a new means of controlling and manipulating spin and valley information. Interfacing graphene with TMDCs can be utilized for novel spin filters, for direct electric-field tuning of the propagation of spins and for implementing spin/valleytronic devices in which charge, spin and valley degrees of freedom can be simultaneously used, as previously proposed for TMDCs [16]. This is thus an important milestone for next-generation graphene-based electronics and computing.

I. METHODS

Device Fabrication. Graphene/WS₂ heterostructures were fabricated by dry viscoelastic stamping [23]. The experimental setup used to transfer two-dimensional crystals comprises an op-

tical microscope with large working distance optical objectives (Nikon Eclipse LV 100ND) and a three axis micrometer stage to accurately position the stamp. Graphene flakes are obtained by mechanical exfoliating highly-oriented pyrolytic graphite (SPI Supplies) onto a p -doped Si/SiO₂ substrate. The single-layer graphene flakes are selected by optical contrast after a previous calibration with Raman measurements. The WS₂ flakes are transferred onto the stamp made of commercially available viscoelastic material (Gelpack) by exfoliation with tape, the surface of the stamp is inspected under the optical microscope to select thin and narrow flakes due to their faint contrast under normal illumination. The WS₂ flake on the stamp is aligned on top of the graphene target with the help of the micrometer stage, then it is pressed against the substrate and peeled off slowly. After assembling, the stacks are annealed for 1 hour at 400 °C, one batch in ultra-high vacuum (10^{-10} Torr) and another in high vacuum (10^{-7} Torr). Annealing removes contamination between the layers as well the remaining residues from the transfer process. The two batches of samples do not show significant differences in terms of mobility and doping. In our devices we define the contact electrodes in one (two) e-beam lithography step(s). To contact the devices all the materials were deposited by e-beam evaporation in a chamber with base pressure of 10^{-8} Torr. For the one-step e-beam lithography case, we deposited TiO₂/Co (1 nm/40 nm) for all the contacts. For the two-step e-beam lithography case, we deposited Ti/Pd for the outer contacts (normal metal) and TiO₂/Co for the inner contacts (ferromagnetic metal, F1 and F2). The widths of the inner ferromagnetic electrodes were 100 and 200 nm to ensure different coercive fields.

Electrical characterization. The devices are wired to a chip carrier that is placed in a cryostat. A rack-and-pinion actuator is used to change the relative angle between the chip carrier and the homogenous applied magnetic field with precision of 0.2°. All the data was acquired at 300 K and under a pressure of 10^{-6} Torr. We characterize the graphene and graphene/WS₂ charge transport properties by means of two- and four-terminal measurements. The contact resistance in the TiO₂/Co electrodes are larger than 10 kΩ. The typical average electron/hole mobility of our devices is in the range of $\mu = 10000 \text{ cm}^2\text{V}^{-1}\text{s}^{-1}$ and the residual carrier density is of the order of $\sim 10^{11} \text{ cm}^{-2}$.

[1] Han W., Kawakami, R. K., Gmitra, M. & Fabian, J. Graphene spintronics. *Nat. Nanotech.* **9**, 794-807 (2014).

- [2] Roche, S. *et al.* Graphene spintronics: the European flagship perspective. *2D Mater.* **2**, 030202 (2015).
- [3] Sander, D. *et al.* The 2017 magnetism roadmap. *J. Phys. D: Appl. Phys.* **00**, 0000 (2017).
- [4] Drögeler, M., Franzen, C., Volmer, F., Pohlmann, T., Banszerus, L., Wolter, M., Watanabe, K., Taniguchi, T., Stampfer, C., & Beschoten, B. Spin lifetimes exceeding 12 ns in graphene nonlocal spin valve devices. *Nano Lett.* **16**, 3533-3539 (2016).
- [5] Roche, S., & Valenzuela, S. O. Graphene spintronics: puzzling controversies and challenges for spin manipulation. *J. Phys. D: Appl. Phys.* **47**, 094011 (2014).
- [6] Gmitra, M., Kochan, D., Högl, P. & Fabian, J. Trivial and inverted Dirac bands and the emergence of quantum spin Hall states in graphene on transition-metal dichalcogenides. *Phys. Rev. B* **93**, 155104 (2016).
- [7] Avsar, A., Tan, J. Y., Taychatanapat, T., Balakrishnan, J., Koon, G.K.W., Yeo, Y., Lahiri, J., Carvalho, A., Rodin, A. S., O'Farrell, E.C.T., Eda, G., Castro Neto, A. H. & Özyilmaz, B. Spin-orbit proximity effect in graphene. *Nat. Commun.* **5**, 4875 (2014).
- [8] Wang, Z., Ki, D.-H., Chen, H., Berger, H., MacDonald, A. H. & Morpurgo, A. F. Strong interface-induced spinorbit interaction in graphene on WS₂. *Nat. Commun.* **6**, 8339 (2015).
- [9] Yan, W., Txoperena, O., Llopis, R., Dery, H., Hueso, L. E. & Casanova, F. A. two-dimensional spin field-effect switch. *Nat. Commun.* **7**, 13372 (2016).
- [10] Dankert, A. & Dash, S. P. Electrical gate control of spin current in van der Waals heterostructures at room temperature. *Nat. Commun.* **8**, 16093 (2017).
- [11] Raes, B., Scheerder, J. E., Costache, M. V., Bonell, F., Sierra, J. F., Cuppens, J., Van de Vondel, J., & Valenzuela S. O. Determination of the spin-lifetime anisotropy in graphene using oblique spin precession. *Nat. Commun.* **7**, 11444 (2016).
- [12] Raes, B., Cummings, A., Bonell, F., Costache, M. V., Sierra, J. F., Roche, S., & Valenzuela S. O. Spin precession in anisotropic media. *Phys. Rev. B* **95**, 085403 (2017).
- [13] Wang, Q. H., Kalantar-Zadeh, K., Kis, A., Coleman, J. N., & Strano, M. S. Electronics and optoelectronics of two-dimensional transition metal dichalcogenides. *Nat. Nanotech.* **7**, 699712 (2012).
- [14] Xiao, D., Liu, G.-B., Feng, W., Xu, X., & Yao, W. Coupled spin and valley physics in monolayers of MoS₂ and other group-VI dichalcogenides. *Phys. Rev. Lett.* **108**, 196802 (2012).

- [15] Yang, L., Sinitsyn, N. A., Chen, W., Yuan, J., Zhang, J., Lou, J. & Crooker, S.A. Long-lived nanosecond spin relaxation and spin coherence of electrons in monolayer MoS₂ and WS₂. *Nat. Phys.* **11**, 830-834 (2015).
- [16] Ye, Y., Xiao, J., Wang, H., Ye, Z., Zhu, H., Zhao, M., Wang, Y., Zhao, J., Yin, X., & Zhang, X. Electrical generation and control of the valley carriers in a monolayer transition metal dichalcogenide. *Nat. Nanotechnol.* **11**, 598-602 (2016).
- [17] Rivera, P., Seyler, K. L., Yu, H., Schaibley, J.R., Yan, J., Mandrus, D.G., Yao, W., Xu, X. Valley-polarized exciton dynamics in a 2D semiconductor heterostructure. *Science* **351**, 688-691 (2016).
- [18] Gmitra, M. & Fabian, J. Graphene on transition-metal dichalcogenides: A platform for proximity spin-orbit physics and optospintronics. *Phys. Rev. B* **92**, 155403 (2015).
- [19] Wang, Z., Ki, D.-H., Hhoo, J. Y., Mauro, D., Berger, H., Levitov, L. S. & Morpurgo, A. F. Origin and magnitude of designer spin-orbit interaction in graphene on semiconducting transition metal dichalcogenides. *Phys. Rev. X* **6**, 041020 (2016).
- [20] Cummings, A., García, J. H., Fabian, J., & Roche, S. Giant spin lifetime anisotropy in graphene induced by proximity effects. *arXiv:1705.10972v1* [cond-mat.mes-hall].
- [21] Johnson, M. & Silsbee, R.H. Interfacial charge-spin coupling: Injection and detection of spin magnetization in metals. *Phys. Rev. Lett.* **55**, 1790 (1985).
- [22] Jedema, F. J., Filip, A. T., & van Wees B. J. Electrical spin injection and accumulation at room temperature in an all-metal mesoscopic spin valve. *Nature* (London) **410**, 345 (2001).
- [23] Castellanos-Gomez, A., Buscema, M., Molenaar, R., Singh, V., Janssen, L., van der Zant, H.S.J. & Steele, G.A. Deterministic transfer of two-dimensional materials by all-dry viscoelastic stamping. *2D Mater.* **1**, 011002 (2015).

Acknowledgments We thank D. Torres for help in designing Fig. 1 and A. Cummings, S. Roche and M. Timmermans for discussions. This research was partially supported by the European Research Council under Grant Agreement No. 308023 SPINBOUND, by the European Union’s Horizon 2020 research and innovation programme under grant agreement No. 696656, by the Spanish Ministry of Economy and Competitiveness, MINECO (under Contracts No MAT2016-75952-R and Severo Ochoa No. SEV-2013-0295), and by the CERCA Programme and the Secretariat for Universities and Research, Knowledge Department of the Generalitat de Catalunya 2014 SGR 56.

J.F.C. acknowledges support from the MINECO Juan de la Cierva program and M.V.C. and F.B. from the MINECO Ramón y Cajal program.

Author contributions L.A.B., J.F.S., W.S.T. and A.A. fabricated the devices and L.A.B., J.F.S. and W.S.T. performed the measurements. F.B. helped with the device fabrication and M.V.C. with the device fabrication and measurements. L.A.B. and S.O.V. analyzed the data and wrote the manuscript. All authors discussed the results and commented on the manuscript. S.O.V supervised the work.

Additional Information The authors declare no competing financial interests. Reprints and permissions information is available online at <http://npg.nature.com/reprintsandpermissions>. Correspondence and request for materials should be addressed to L.A.B. (antonio.benitez@icn2.cat) and S.O.V. (SOV@icrea.cat).

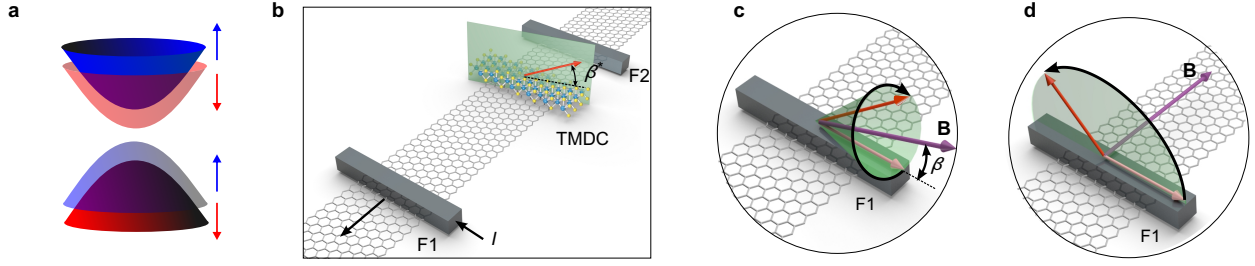


FIG. 1. **Proximity-induced spin-orbit coupling and measurement scheme.** **a**, Representation of the graphene (gr) electronic band structure in the vicinity of the Dirac point for gr/WS₂. The colors and arrows represent the expectation value for the out-of-plane spin component. **b**, Schematics of the device design and measurement approach. The device consists of a graphene channel contacted with two ferromagnets (F1 and F2) and a transverse strip of WS₂ in between. A charge current (straight black arrows) through F1 injects spins having an orientation parallel to the F1 magnetization direction. The injected spins undergo Larmor precession under the influence of a magnetic field B while diffusing towards the detector electrode (F2) (see **c** and **d**). When a spin reaches the location of WS₂, its orientation is characterized by the angle β^* , which measures the inclination of the spin from the graphene plane. Owing to the anisotropic band structure of graphene/WS₂, the spin signal detected at F2 is modulated by B . **c**, Out-of-plane spin precession with oblique magnetic field B , where B is applied in a plane that contains the easy axis of the ferromagnetic electrodes and that is perpendicular to the substrate. **d**, Out-of-plane spin precession with in-plane B with B perpendicular to the length of F1 and F2. Spins precess in a plane perpendicular to the substrate. In **c** and **d**, the effective spin lifetime becomes sensitive to both parallel and perpendicular spin lifetimes, $\tau_{s\parallel}$ and $\tau_{s\perp}$, and the spin relaxation anisotropy can be experimentally obtained.

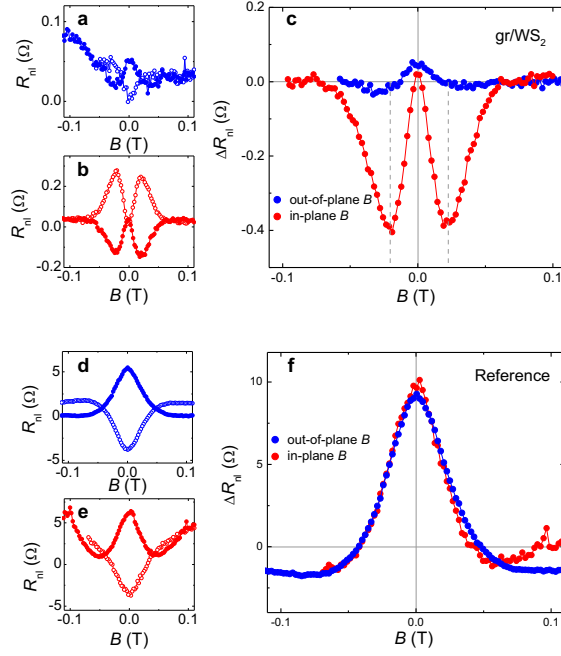


FIG. 2. Spin relaxation anisotropy. Non-local resistance R_{nl} versus B with different B orientation. The measurements in **a-c** are for a gr/WS₂ device while those in **d-f** are for a reference device (without WS₂) in the same graphene flake. **a, d**, Standard spin precession measurements with B perpendicular to the substrate. Solid (open) symbols are for parallel (antiparallel) configurations of the magnetizations of F1 and F2 (R_{nl}^+ and R_{nl}^- , respectively). The gr/WS₂ (**a**) and reference (**d**) show qualitatively the same response, although the magnitude of R_{nl} in the former is significantly smaller. **b, e**, Spin precession measurements with B in the graphene plane as represented in Fig. 1d. Solid and open symbols are for parallel and antiparallel configurations. The gr/WS₂ (**b**) and reference (**e**) display different behaviour. R_{nl} in the reference device does not vary with B orientation, neither in magnitude nor in the precession features. In the gr/WS₂ device R_{nl} increases in magnitude when spins rotate out of the graphene plane, rapidly changing sign; R_{nl} presents extrema at $B \sim \pm 20$ mT with a magnitude that exceeds $|R_{nl}(B = 0)|$. **c, f**, $\Delta R_{nl} = R_{nl}^+ - R_{nl}^-$ versus B as extracted from **a, b** and **d, e**. The blue (red) plots are for perpendicular (in-plane) B . The dashed lines in **c** mark the position of the extrema for the measurements with in-plane B . $T = 300$ K; $I = 2 \mu\text{A}$.

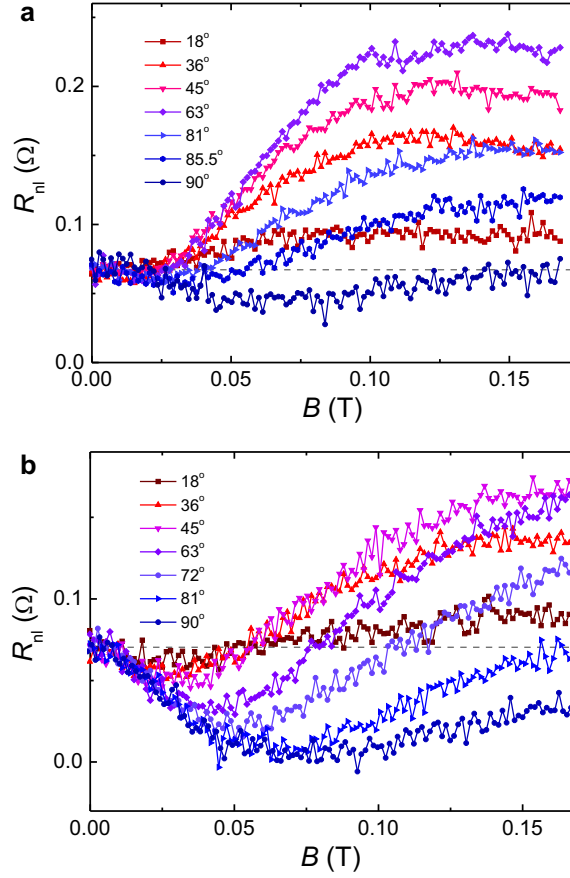


FIG. 3. **Spin precession measurements under oblique magnetic fields.** **a**, Representative subset of experimental spin precession curves for the indicated β as a function of B , when F1 is used as spin injector. The precession data are acquired after preparing a parallel magnetization configuration of F1 and F2. Dephasing of the precessing component is observed at B larger than ~ 0.12 T. The horizontal dashed line is the non-local resistance at $B = 0$, R_{nl}^0 , which coincides with R_{nl} at $\beta = 0^\circ$ in the parallel configuration. Similarly to Fig. 2b, R_{nl} surpasses R_{nl}^0 as soon as the spins rotate out-of-plane. **b**, Representative subset of experimental spin precession curves for the indicated β at a function of B when F2 is used as spin injector. Because gr/WS₂ is close to the injector, dephasing of the precessing component is not achieved at its location and R_{nl} becomes dependent of B in the full B range. $T = 300$ K, $V_g = -15$ V and $I = 2 \mu\text{A}$.

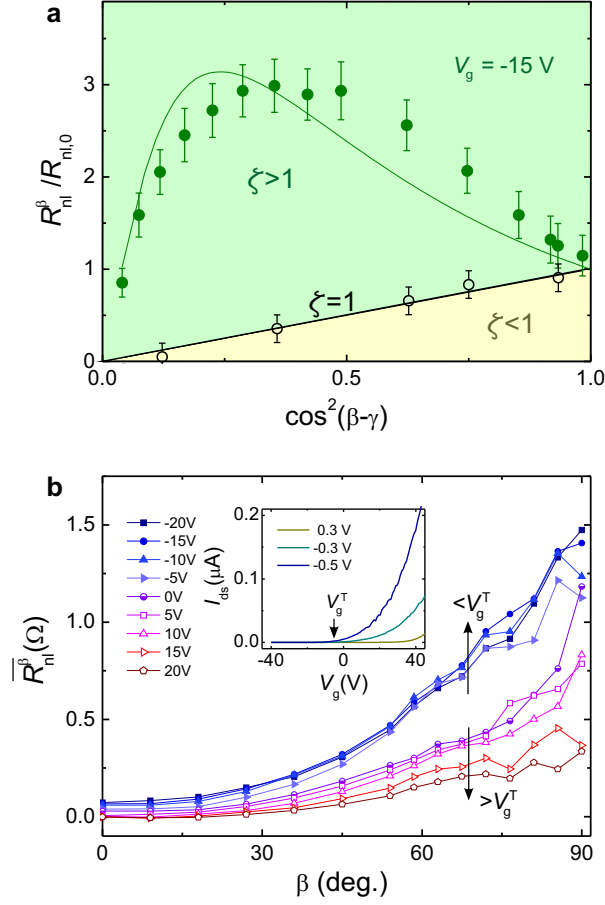


FIG. 4. **Spin lifetime anisotropy ratio, ζ .** **a**, R^{β}_{ni} normalized by $R_{ni,0}$ as a function of $\cos^2(\beta - \gamma)$, with $\gamma = \gamma(\beta, B)$. The data represented by solid symbols are extracted from Fig. 3a at $B = 0.16$ T. The error bars derive from the noise in Fig. 3a. The solid green line represents the modeled response for an anisotropy ratio $\zeta = 10$. The data represented by open symbols are extracted from Supplementary Fig. 4 and correspond to a reference device. In this case, $\zeta \approx 1$, as shown by the straight black line. **b**, $\overline{R^{\beta}_{ni}}$ as a function of β for the indicated back-gate voltages V_g . For $V_g < V_g^T \approx -5$ V, $\overline{R^{\beta}_{ni}}$ is independent of V_g but decreases rapidly for $V_g > V_g^T$. Inset, Transfer characteristics I_{ds} versus V_g for different bias voltage V_{ds} in gr/WS₂; V_g^T coincides with the back-gate voltage at which I_{ds} is observed.